MALAYSIAN JOURNAL OF ANALYTICAL SCIENCES

Journal homepage: https://mjas.analis.com.my/

Research Article

Catalytic activation of peroxymonosulfate with Mn and N co-doped carbon allotropes for alizarin yellow R degradation

Ganapaty Manickavasagam, Wen-Da Oh*, and Mardiana Saaid

School of Chemical Sciences, Universiti Sains Malaysia, 11800 Penang, Malaysia

*Corresponding author: ohwenda@usm.my

Received: 28 August 2025; Revised: 4 November 2025; Accepted: 15 November 2025; Published: 28 December 2025

Abstract

Transforming waste into catalysts for wastewater treatment embodies the circular economy concept and provides a sustainable approach to eliminate recalcitrant azo dyes. In this study, carbon nanotubes (CNTs) and biochar (BC) co-doped with Mn and N (i.e., Mn-N-CNT-1 and Mn-N-BC-1, respectively), along with their control forms (i.e., X, N-X, and Mn-X-1, X = CNT or BC), were synthesized via the pyrolysis method and systematically compared in terms of peroxymonosulfate (PMS) activation performance for alizarin yellow R (AYR) degradation, underlying mechanisms, stability, and phytotoxicity. X-ray diffraction (XRD) analysis revealed that Mn-N-CNT-1 exhibited a higher degree of graphitization than Mn-N-BC-1, while no crystalline Mn or Mn oxide phases were detected. Catalytic performance studies revealed that CNT co-doped with Mn and N possesses superior ability to degrade AYR (pseudo first-order rate constant (k_{app}) = 0.042 min^{-1}, 84.6 % removal) compared to controls and BC-based catalysts. Quenching experiments identified $SO_4^{\bullet-}$, $^1O_2$, and nonradical electron transfer as the dominant pathways for AYR degradation. Phytotoxicity assays confirmed that catalytic treatment reduced AYR toxicity, enabling normal seed germination and growth. In short, these findings in this study highlight CNT co-doped with Mn and N as efficient, reusable, and environmentally safe PMS activators for sustainable wastewater remediation.

Keywords: wastewater treatment, peroxymonosulfate activation, azo dye, biochar, carbon nanotubes

Introduction

Paper, food, leather goods, plastics, and textile industries are industrial wastewater sources, generating significant quantities of dyestuff each year (approximately 2.8×10^5) [1]. Among the dyestuffs, azo dyes represent the most commonly used class of synthetic colorants, with more than three thousand different types applied in textile production and printing [2]. 5-[(p-Nitrophenyl)azo]salicylic acid sodium salt, commonly known as alizarin yellow R (AYR), is a water-soluble anionic azo dye characterized by the presence of polycyclic aromatic hydrocarbons in its molecular structure. In addition to its widespread application in textile dyeing, AYR is also employed as an acid-base indicator [3]. Due to their complex aromatic structures, azo dyes have poor biodegradability, contributing to their long-term persistence in aquatic environments [4]. In addition to their environmental persistence, these dyes are associated with high toxicity levels and potential carcinogenic effects [5]. As a result, it is essential to eliminate them from wastewater before it is discharged into natural water bodies. Advanced oxidation processes (AOPs) remain the most widely applied method among the various treatment approaches due to their effectiveness in degrading recalcitrant pollutants and continue to be a major focus of current research.

In recent years, peroxymonosulfate-based AOPs (PMS-AOPs) have garnered attention from researchers due to their ability to be activated via both radical and nonradical pathways, such as sulfate radicals ($SO_4^{\bullet-}$, 2.5 – 3.1 V NHE), hydroxyl radicals ($^{\bullet}OH$, 2.8 V NHE), singlet oxygen ($^1O_2$, 1.52 V NHE), high-valent metal species, electron transfer processes, and surface-activated complexes, enabling the effective degradation of recalcitrant pollutants [7,6]. However, PMS requires activation to generate radicals, which can be achieved through both homogeneous and heterogeneous catalytic processes. Homogeneous activation typically involves transition metal ions such as Co^{n+}, Mn^{n+}, and Fe^{n+}, while heterogeneous activation employs solid-phase catalysts, including carbon-based materials, metal-organic frameworks (MOFs), single or mixed transition metals, etc [8]. Heterogeneous catalysts are often chosen over homogeneous ones because the

latter come with several challenges in real applications, such as (a) formation of metal-containing sludge, which requires additional steps for removal and proper disposal, (b) high sensitivity to changes in pH, which leads to the hydrolysis of metal ions or formation of precipitates, and (c) the use of metal salts introduces additional anion ions (e.g., SO_4^{2-} and Cl^-) into the reaction solution and reduces the effectiveness of catalytic performance [9]. In contrast, heterogeneous catalysts offer several key advantages for the activation of PMS, such as (a) oxidants can be effectively without the need for external energy input, (b) reduce the risk of secondary contamination, (c) capable of functioning under a broad range of operating conditions, (d) catalysts can be readily separated from the reaction medium, and (e) reusability [10]. Carbon-based catalysts have gained attention due to their tunable physicochemical properties and environmental friendliness [11]. Nevertheless, the limited availability of active sites for PMS activation on pristine carbon-based catalysts significantly constrains their practical application in environmental remediation [12]. The co-doping strategy involving metals and heteroatoms has proven effective in creating active sites by modifying the internal chemical structure of carbon-based catalysts.

Several heteroatoms have been reported for co-doped carbon-based catalysts, including N [13], B [14], P [15], S [16], and O [17]. Among these, N doping is particularly attractive because it can induce the formation of various N moieties, such as pyridinic N, graphitic N, pyrrolic N, and N oxide. The incorporation of these N species not only generates abundant structural defects but also enhances the electronic conductivity of the carbon matrix [18]. Notably, pyridinic N, graphitic N, and pyrrolic N have been reported to effectively activate PMS, thereby significantly improving the catalytic activity of carbon-based catalysts [19]. Mn is selected for co-doping with N due to its rich redox chemistry and multiple oxidation states, which enable it to participate in diverse and continuous redox reactions, promoting the generation of reactive oxygen species [20]. In our previous study, we evaluated the catalytic performance of char-type (biochar (BC) and hydrochar (HC)) carbon-based catalysts co-doped with metal and heteroatom for the degradation of norfloxacin. The results revealed that BC-based catalysts exhibited superior performance compared to HC-based catalysts, primarily due to their higher electrical conductivity and larger specific surface area [21]. Although biochar-based catalysts have proven effective, there remains a need to explore other carbon materials with distinct structural and electronic characteristics. In particular, carbon nanotubes (CNTs) can be a suitable carbon allotrope selection due to their unique stacking morphology and well-defined tubular structure, which can markedly increase the surface area and facilitate the uniform dispersion of active sites [22]. Additionally, the surface electronic properties of CNTs can significantly influence the configuration and activity of metal-heteroatom coordination sites, thereby enhancing the PMS activation efficiency [23].

Herein, this study aims to synthesize Mn, N co-doped CNT (Mn-N-CNT) along with corresponding control samples, including non-doped CNT, N-doped CNT, and Mn-doped CNT. The synthesis was performed using a two-step pyrolysis method. In the first step, CNT was synthesized, followed by a second step involving the co-doping of Mn and N onto the CNT framework. Subsequently, the catalytic performance of the synthesized materials is assessed through their ability to activate PMS for the degradation of AYR and physicochemical properties associated with superior catalytic performance are discussed. The influence of various operational parameters, including initial pH, catalyst loading, and PMS dosage, on the degradation rate of AYR through PMS activation was systematically evaluated. Thereafter, quenching experiments were conducted using the as-prepared catalyst to elucidate the underlying activation mechanism. To evaluate the practical applicability of the catalyst, its stability was assessed through a reusability test. Lastly, a phytotoxicity study was performed to examine the toxicity of the treated AYR solution.

Materials and Methods

Chemicals

Sawdust was obtained from a factory located in Ipoh, Perak. AYR ($C_{13}H_9N_3O_5$, Bendosen), polyethylene glycol 6000 (PEG6000, $H(OCH_2CH_2)_nOH$, BDH), calcium nitrate tetrahydrate ($Ca(NO_3)_2{\cdot}4H_2O$, Chemiz), ammonium molybdate tetrahydrate ($(NH_4)_6Mo_7O_{24}{\cdot}4H_2O$, ChemAR), nickel(II) nitrate hexahydrate ($Ni(NO_3)_2{\cdot}6H_2O$, Fisher Scientific), manganese nitrate tetrahydrate ($Mn(NO_3)_2{\cdot}4H_2O$, Sigma-Aldrich), potassium peroxymonosulfate ($2KHSO_5{\cdot}KHSO_4{\cdot}K_2SO_4$, ACRÕS), hydrochloric acid (HCl, QRëC), sodium hydroxide (NaOH, Systerm®), tert-butanol (TBA, $(CH_3)_3COH$, EMSURE®), ethanol (EtOH, C_2H_5OH, Chemiz), sodium azide (NaN_3, RandM Chemicals), and sodium perchlorate monohydrate ($NaClO_4$, Sigma-Aldrich). Deionized (DI) water was used to conduct all the experiments.

Synthesis of carbon nanotubes

CNTs were synthesized using a NiMoCa catalyst [24]. Briefly, 0.2 g of PEG600, 0.33 g of Ca salt, 0.13 g of Mo salt, and 1.54 g of Ni salt were dissolved in 40 mL of DI water and the resulting mixture solution was calcined in a muffle furnace (Carbolite Gero Ltd.) at 650 °C for 10 min and with a ramping rate of 10 °C min^{-1}. The calcined product was then collected, thoroughly washed with DI water, and dried at 60 °C before use. Subsequently, 0.05 g of NiMoCa catalyst

was mixed with 1.62 g of sawdust in a porcelain crucible and wrapped with several layers of aluminum foil to create an inert atmosphere. The mixture was then pyrolyzed at 600 °C for 10 min with a heating rate of 10 °C min^{-1}. The black powder was subjected to acid digestion using 3 N hydrochloric acid and then washed with DI water. The resultant catalyst was designated as CNT. The schematic illustration of the preparation process is shown in **Figure 1**.

Synthesis of Mn, N co-doped carbon nanotubes

Co-doped CNT was prepared by mixing 0.1 g of CNT, 1.0 g of urea, and 1.0 wt% of Mn in a porcelain crucible and wrapped with several layers of aluminium foil. The mixture was then pyrolyzed at 800 °C for 1 h with a heating rate of 10 °C min^{-1}. The resultant catalyst was washed with DI and designated as Mn-N-CNT-1. The same catalyst was prepared with different wt% of Mn (i.e., 0.5, 2.0, and 3.0) and designated as Mn-N-CNT-0.5, Mn-N-CNT-2, and Mn-N-CNT-3. Control catalysts doped individually with either Mn or N were synthesized under similar conditions and designated as Mn-CNT-1 and N-CNT, respectively.

Synthesis of Mn, N co-doped biochar

Co-doped BC was prepared by mixing 0.1 g of sawdust, 1.0 g of urea, and 1.0 wt% of Mn in an alumina crucible and wrapped with 10 layers of aluminium foil. The mixture was then pyrolyzed at 800 °C for 1 h with a heating rate of 10 °C min^{-1}. The resultant catalyst was washed with DI and designated as Mn-N-BC-1. Control catalysts doped individually with either Mn or N were synthesized under similar conditions and designated as Mn-BC-1 and N-BC, respectively. The non-doped biochar was designated as BC.

Characterizations

The surface morphology of the catalyst was investigated using FESEM (Field emission scanning electron microscopy, FEI Quanta 650 FEG), while the elemental composition was determined using Energy dispersive X-ray spectroscopy (EDX, Oxford Instruments). The surface chemistry of the catalyst was studied using Fourier transform infrared spectroscopy (FTIR, Shimadzu). The crystal phase of the catalyst was investigated using the X-ray diffractometer (XRD, Bruker AXS D8 ADVANCE) with Cu-Kα radiation (λ = 1.5418 Å). The degree of graphitization and defects was determined using Raman spectrometer (Renishaw inVia, United Kingdom). Thermal properties of the catalyst were investigated using thermogravimetric analysis (TGA, PerkinElmer thermal analyzer). The point of zero charge of the catalyst was determined using the pH drift method.

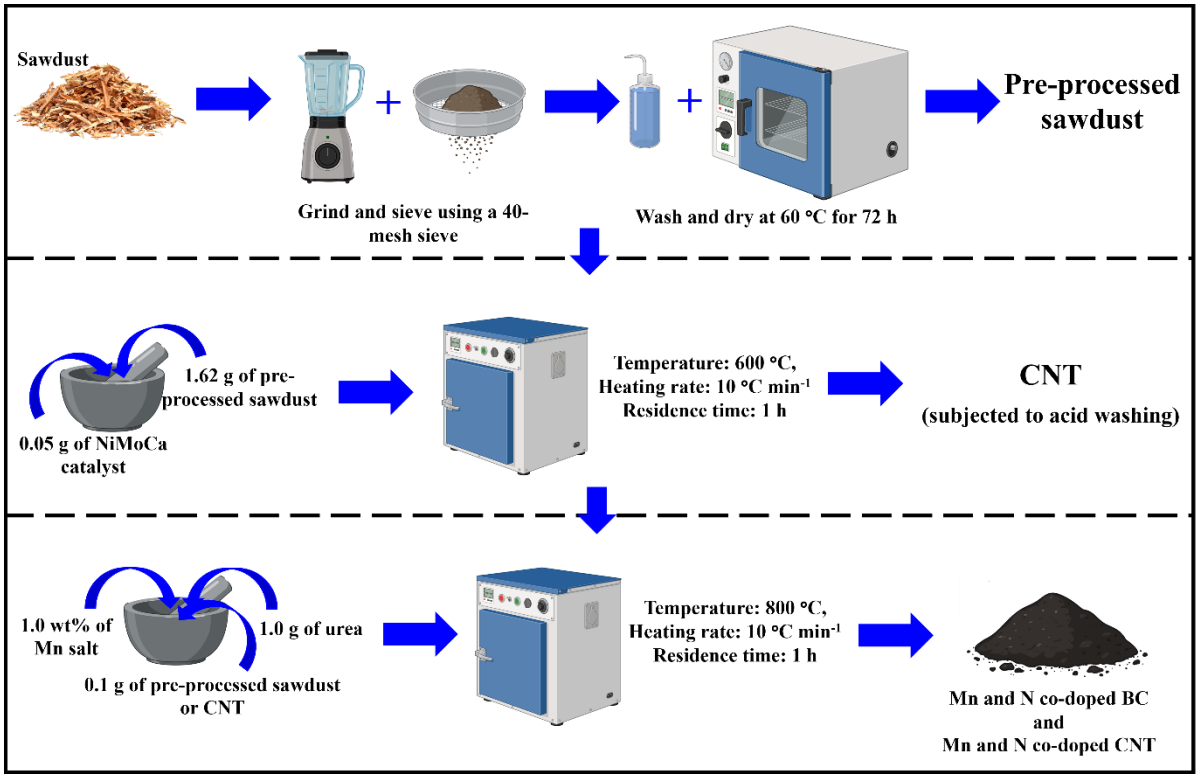

Figure 1. Schematic representation of the preparation process for BC and CNT co-doped with Mn and N

Evaluation of catalytic performance

AYR was used as a model pollutant to determine the catalytic performance of as-prepared catalysts. Briefly, a beaker containing 10 mg L^{-1} of AYR, 0.30 g L^{-1} of PMS, and 0.30 g L^{-1} of catalyst was prepared and the degradation of AYR was monitored for a duration of 45 min with an interval of 5 min. The changes in the concentration of AYR were determined at λ_{max} = 318 nm using UV–Vis spectrophotometer (Shimadzu 2600 UV–Vis). Besides, the catalytic performance of the optimal catalyst was determined in different operation conditions, such as pH (3 – 9), PMS dosage (0.15 – 0.60 g L^{-1}), and catalyst loading (0.15 – 0.60 g L^{-1}). Quenching experiment was performed using four different quenchers (i.e., TBA, EtOH, NaN_3, and $NaClO_4$) to determine the contribution of radical and nonradical pathways in the AYR degradation mechanism. The reusability test of the optimal catalyst was determined for five consecutive cycles. The spent catalyst from each cycle was filtered, washed, and dried prior to use in the subsequent cycle. As for the fifth cycle, the spent catalyst from the fourth cycle was regenerated at 450 °C for 2 h at a heating rate of 10 °C min^{-1} under an oxygen-limited atmosphere. The total organic carbon (TOC) of untreated and treated water was determined using a TOC analyzer (Shimadzu). Mn leaching was investigated using an atomic absorption spectrometer (AAS 400). The toxicity effect of the control, untreated, and treated water was evaluated using a phytotoxicity assessment.

Results and Discussion

Characterizations

FESEM-EDX analysis was employed to verify the successful synthesis of CNT and the effective incorporation of Mn and N dopants. As shown in **Figure 2**, FESEM images confirm that Mn-N-CNT-1 maintains a characteristic nanotubular morphology. Elemental mapping of the catalyst demonstrates a uniform dispersion of both Mn and N, confirming their successful co-doping within the framework. Quantitative analysis further indicated that the Mn and N contents in Mn-N-CNT-1 were 0.21 and 3.28 wt%, respectively.

The crystal phase of the catalysts was studied using XRD. The XRD pattern of Mn-N-CNT-1 and Mn-N-BC-1 in **Figure 3a** shows that both catalysts have major peaks at 20-26° and 43-46° corresponding to the (002) and (101) planes of the carbon structure [25], respectively. However, these peaks are generally broader in Mn-N-BC-1 and sharper in Mn-N-CNT-1. This trend signifies that Mn-N-CNT-1 possesses a higher extent of carbon structure graphitization than Mn-N-BC-1 [26]. Also, no significant peaks attributed to the metallic Mn or oxide forms of Mn (e.g., MnO, MnO_2, and Mn_3O_4) were observed [27].

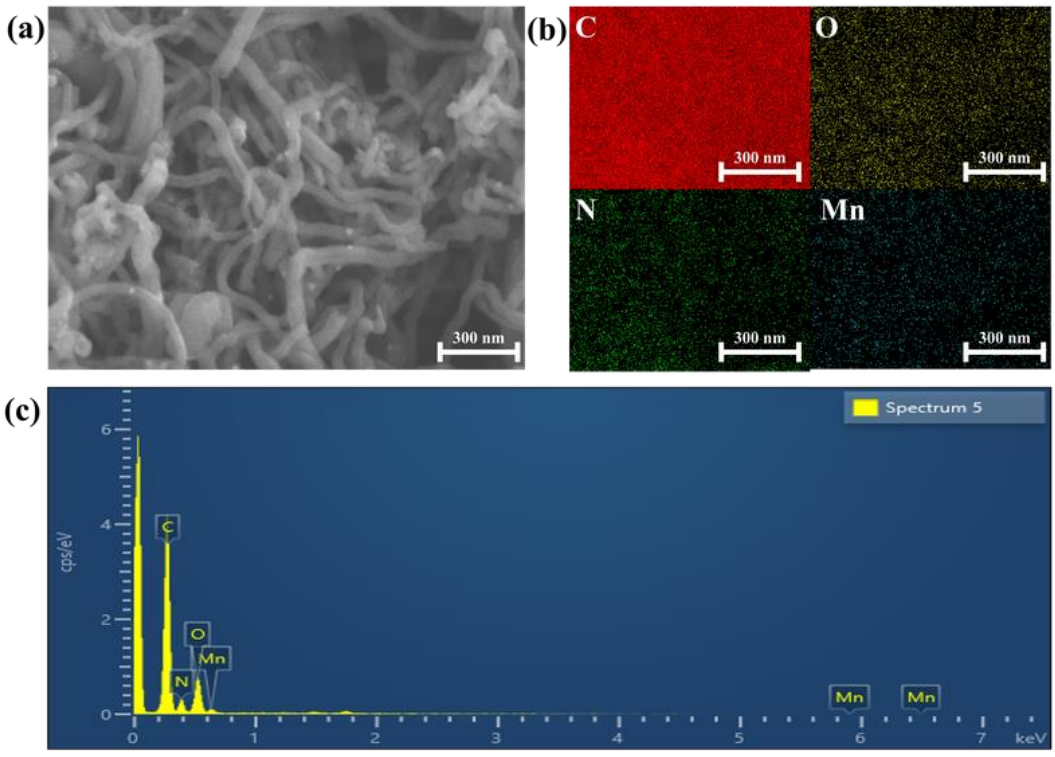

Figure 2. (a) FESEM of Mn-N-CNT-1 (at magnification of 150065×), (b) elemental mapping of C, O, N, and Mn in Mn-N-CNT-1, and (c) EDX spectrum of Mn-N-CNT-1

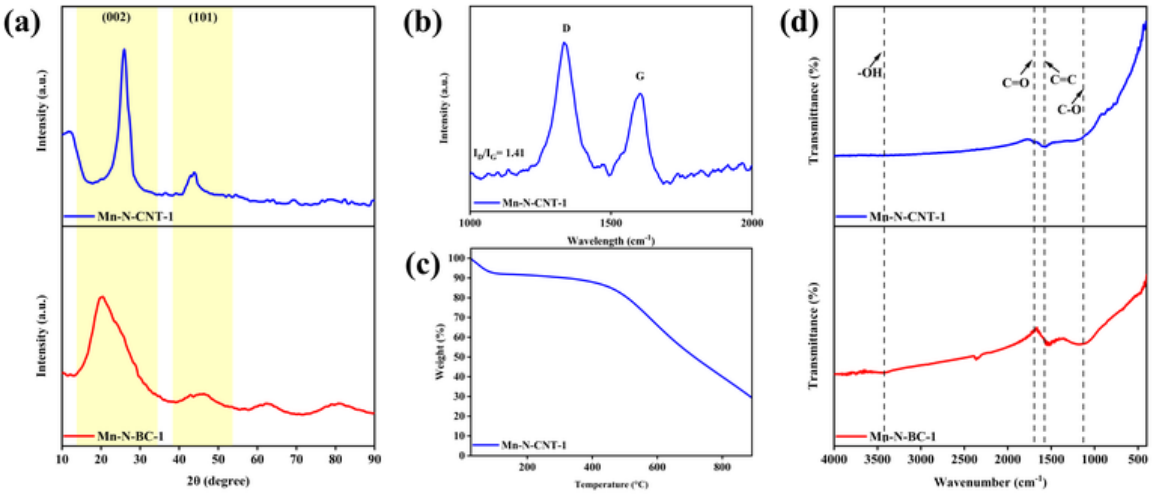

Figure 3. (a) XRD pattern, (b) Raman spectrum, (c) TGA pattern, and (d) FTIR spectra of as-prepared catalysts

The degree of graphitization and defects of the catalyst were studied using Raman analysis. **Figure 3b** represents the Raman spectrum of Mn-N-CNT-1. The D-band at ~1340 cm^{-1} represents disordered carbon arising from defective structure, while G-band at ~1580 cm^{-1} represents graphitized carbon [12]. The I_D/I_G ratio of >1.0 signifies that the catalyst is composed of a high degree of structural defects. The doping process with external dopants can reconstruct the carbon structure and result in high structural defects [12]. Defective structures are usually in an electron-loss state and have great potential in absorbing PMS and obtaining electrons from the PMS via the electron transfer process [12].

The thermal stability of the as-catalyst was studied using TGA and the TGA pattern of Mn-N-CNT-1 is illustrated in **Figure 3c**. The weight loss of ~8% at <130 °C is attributed to the removal of moisture content and adsorbed water [28]. The ~4% weight loss at <400 °C is due to the removal of volatile matter. The drastic weight loss was observed at >500 °C only because the incorporation of Mn and N into the CNT framework enhances thermal tolerance by stabilizing the carbon lattice and improving its resistance to combustion reactions. The drastic weight loss is attributed to the decomposition of the carbon structure of CNT into CO_x. Also, the results indicate that the as-prepared catalyst can be regenerated at <500 °C without undergoing significant structural decomposition and weight loss.

The surface chemistry of the as-prepared catalysts was examined by FTIR spectroscopy and the corresponding spectra are presented in **Figure 3d**. Overall, only minor differences in surface functionalities were detected among the samples, yet some distinct features are noteworthy. The broad absorption band at ~3400 cm^{-1} is particularly noticeable in Mn-N-BC-1, which can be ascribed to -OH stretching vibrations [29]. The prominence of this band suggests that the BC-based catalyst contains a relatively high density of oxygenated functional groups, such as hydroxyls (-OH), carboxyls (-COOH), and adsorbed water molecules. This observation is consistent with the predominantly amorphous nature of biochar [30]. Besides, the peak at ~1700 cm^{-1} is attributed to C=O stretching [23]. The C=C stretching at ~1580 cm^{-1} and C-O stretching at ~1132 cm^{-1} were observed for both catalysts [31,32]. Oxygen-containing functional groups play a crucial role in enhancing the catalytic potential of carbon materials by promoting PMS activation and strengthening the interactions between metal, heteroatom, and the carbon framework [33]. Previously, oxygen-containing groups, such as -COOH, -C=O, and -C-OH, have been reported to have a role in heterogeneous catalysis processes for the degradation of pollutants [34].

Performance studies

Catalytic performance comparison of different catalysts

The performance of two different carbon allotropes co-doped with Mn and N as PMS activators for the degradation of AYR was investigated. To analyze the kinetics of AYR degradation during the catalysis, the reaction data were fitted using the pseudo-first-order kinetic model (Eq 1).

$$[P]_t = [P]_0 e^{-k_{app} t} \quad (1)$$

where $[P]_0$ represents the initial pollutant concentration (t = 0 min), $[P]_t$ represents pollutant concentration at time t, k_{app} represents pseudo first-order rate constant, and t is the total reaction time.

Initially, the degradation of AYR through direct PMS oxidation was examined and ~ 6% of AYR was degraded. This limited degradation highlights the weak oxidizing ability of PMS without activation and emphasizes the need for a suitable catalyst to enhance the generation of reactive oxygen species and achieve higher removal efficiencies. As shown in **Figure 4a**, the AYR degradation rate by CNT follows the order of CNT (22.6 %, 0.006 min^{-1}) < N-CNT (33.0 %, 0.009 min^{-1}) < Mn-CNT-1 (40.9 %, 0.012 min^{-1}) < Mn-N-CNT-1 (71.3 %, 0.028 min^{-1}). Similarly, the AYR degradation rate by BC (**Figure 4b**) follows the order of BC (10.0 %, 0.002 min^{-1}) < N-BC (22.6 %, 0.006 min^{-1}) < Mn-BC-1 (37.4 %, 0.010 min^{-1}) < Mn-N-BC-1 (53.0 %, 0.017 min^{-1}). The pristine CNT and BC exhibited very limited activity, which can be ascribed to the lack of abundant active sites and the activation mainly depends on electron-deficient carbon, surface functional groups, and the electron-transfer regime [35].

On the other hand, the enhancement by N-doped catalysts is due to the higher degree of nitrogen incorporation. N atoms in carbon materials can exist in several configurations, including pyrrolic N, pyridinic N, graphitic N, and N-oxide. When the synthesis temperature exceeds 700 °C, graphitic N typically becomes the predominant form. This type of nitrogen is particularly important, as it offers thermally stable sites with strong catalytic activity, thereby playing a key role in promoting PMS activation [36]. However, excessively high temperatures (> 900 °C) should be avoided, since they may lead to a severe loss of nitrogen dopants and even partial collapse of the carbon framework, thereby reducing the overall catalytic performance [37]. The incorporation of Mn further boosted the degradation efficiency, as Mn species are well known to act as redox-active centers capable of accelerating PMS decomposition into reactive oxygen species [38]. Subsequently, the dual modification achieved through Mn and N co-doping in Mn-N-CNT-1 and Mn-N-BC-1 led to a further improvement in the degradation rate. This enhancement is likely associated with the synergistic interaction between Mn and N and Mn-N coordination structures, which appears pivotal in facilitating PMS activation and a more efficient generation of reactive oxygen species ROS. For example, biochar co-doped with Fe and N was observed to have a higher removal efficiency of sulfamethoxazole than Fe-doped, N-doped, and non-doped catalysts [39].

When comparing Mn-N-CNT-1 with Mn-N-BC-1, Mn-N-CNT-1 exhibited superior performance in degrading AYR. To ensure that this improvement originated from PMS activation rather than simple adsorption, the activity of Mn-N-CNT-1 was further examined in the absence of PMS. Under these conditions, only ~16.0% of AYR was removed, confirming that adsorption alone could not account for its high degradation efficiency. The superior catalytic performance of Mn-N-CNT-1 compared to Mn-N-BC-1 can likely be attributed to its more favorable textural and electronic properties. The enhanced performance of Mn-N-CNT-1 can be attributed to its nanotubular framework, which possesses lower amorphous content and a higher degree of graphitization compared to biochar [40], which translates into a greater density of stable active sites and reduced susceptibility to self-oxidation.

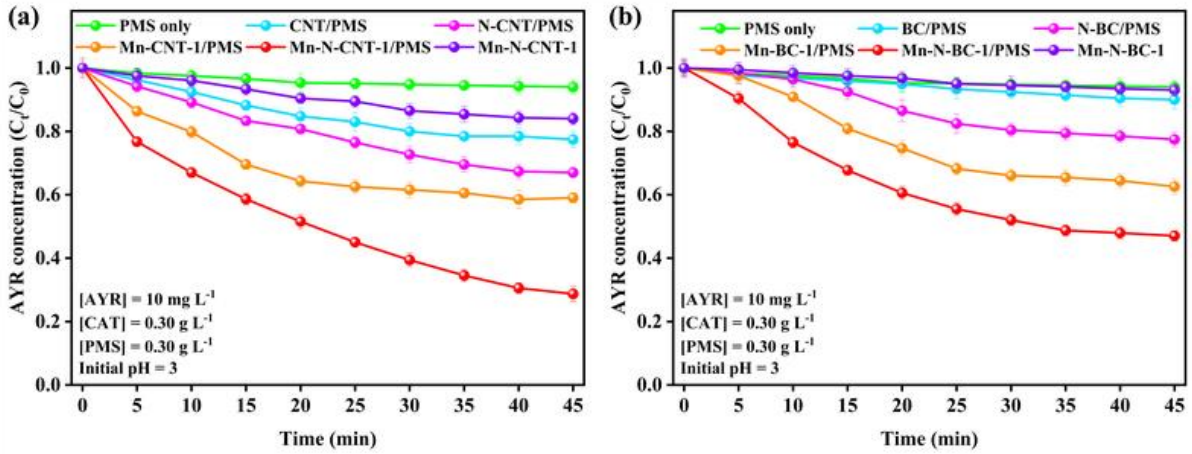

Figure 4. Catalytic performance of (a) CNT and (b) BC in AYR degradation

Influence of operation parameters

Following the identification of the most efficient catalyst, the influence of Mn loading, catalyst dosage, PMS concentration, and initial pH on AYR degradation was examined. An increase in Mn loading from 0.5 wt.% to 3.0 wt.% enhanced the AYR degradation from 0.021 min^{-1} (61.9%) to 0.042 min^{-1} (84.6%) (**Figure 5a**). This enhancement could be attributed to two main factors. Firstly, it is because higher transition metal loading promotes interfacial electron transfer and generates additional structural defects. For example, the increase in Mo content from 0.2 g to 0.4 g in synthesizing Fe/Mo-NC resulted in an enhancement of bisphenol A degradation due to increasing material defects (increase in I_D/I_G ratio from 1.13 to 1.36) and interfacial electron transfer (smaller arc radius of the EIS Nyquist curve) [41]. Besides, an increase in dopant concentration in Fe-NS@C has been reported to increase the defect density and disordered degree of the catalyst, which can enhance the degradation rate of bisphenol A [42]. Secondly, a higher metal loading can result in the formation of more metal-heteroatom coordination sites, which provide stable and efficient centers for PMS activation. For example, in the Cu-N-BC/PMS system used for paracetamol degradation, increasing the Cu loading from 5 mg L^{-1} to 10 mg L^{-1} enhanced the degradation rate [43]. The enhancement was reported due to the synergistic interaction between Cu and N, which is crucial for the formation of the Cu-N structures.

As shown in **Figure 5b**, AYR degradation was strongly influenced by the catalyst loading. Increasing the catalyst loading from 0.15 mg L^{-1} to 0.60 mg L^{-1} led to a noticeable improvement in the degradation rate from 0.020 min^{-1} (58.6 %) to 0.050 min^{-1} (96.6 %). This trend suggests that higher catalyst loading provides more accessible active sites for PMS activation. However, a continuous increase in catalyst loading does not necessarily improve catalytic performance. At higher loadings, the larger number of active sites can promote the generation of more reactive oxygen species [44]. Nevertheless, these species may undergo radical quenching by reacting with other reactive oxygen species or with PMS, thereby reducing their effective contribution to pollutant degradation. For example, increasing the N-doped biochar aerogel loading for PMS activation from 0.3 g L^{-1} to 0.4 g L^{-1} resulted in a declining trend in the degradation rate of bisphenol A [45]. In addition, excessive catalyst loading introduces a greater number of adsorption sites, where pollutants may preferentially accumulate and block the active centers [46]. This blockage further limits PMS activation and decreases the availability of reactive oxygen species, thereby suppressing the overall catalytic efficiency.

Besides, the degradation of AYR is also highly dependent on PMS concentration. When the PMS dosage was increased from 0.15 mg L^{-1} to 0.60 mg L^{-1} (**Figure 5c**), the degradation rate improved from 0.018 min^{-1} (55.5 %) to 0.020 min^{-1} 0.058 min^{-1} (92.8 %), indicating that additional PMS molecules promoted the generation of reactive oxygen species. However, PMS dosage must be carefully monitored, since excessive amounts may quench reactive radicals and increase costs [47].

The effect of the initial pH of the solution on AYR degradation is shown in **Figure 5d**. The degradation of AYR is higher in neutral (pH 7: 0.033 min^{-1} and 77.7%) and basic (pH 9: 0.038 $min^{-1}$and 81.6%) mediums than acidic mediums (pH 3: 0.028 min^{-1} and 71.3% and pH 5: 0.019 min^{-1} and 57.5%). In all tested pH values, no change occurred in the charge of PMS (pKa = 9.4 [48]) and AYR (pKa = 11 [49]), indicating that both species remained positively charged. In contrast, Mn-N-CNT-3 with a point of zero charge (pH_{PZC}) of 6.9 (**Figure 6**), exhibited different surface charges depending on the solution pH. At pH 7 and 9, the catalyst surface was negatively charged, favoring electrostatic attraction with PMS. This facilitated PMS adsorption onto the active sites, thereby enhancing its activation into reactive oxygen species generation. Conversely, the catalyst surface at pH 3 and 5 carried a positive charge, leading to electrostatic repulsion with PMS. Under these conditions, PMS adsorption and activation were less efficient, reducing reactive oxygen species generation and consequently lowering AYR degradation.

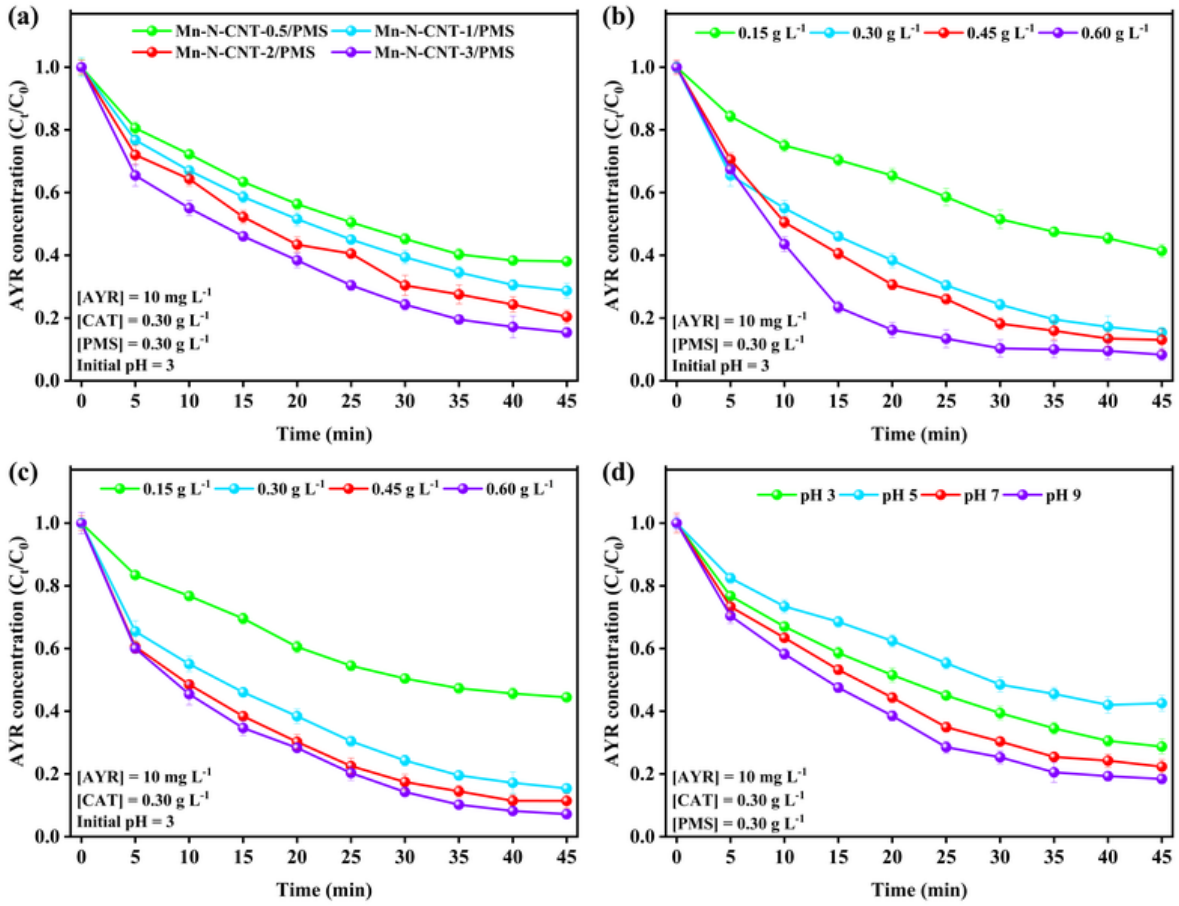

Figure 5. Effect of (a) Mn loading, (b) catalyst loading, (c) PMS dosage, and (d) initial pH on the degradation of AYR

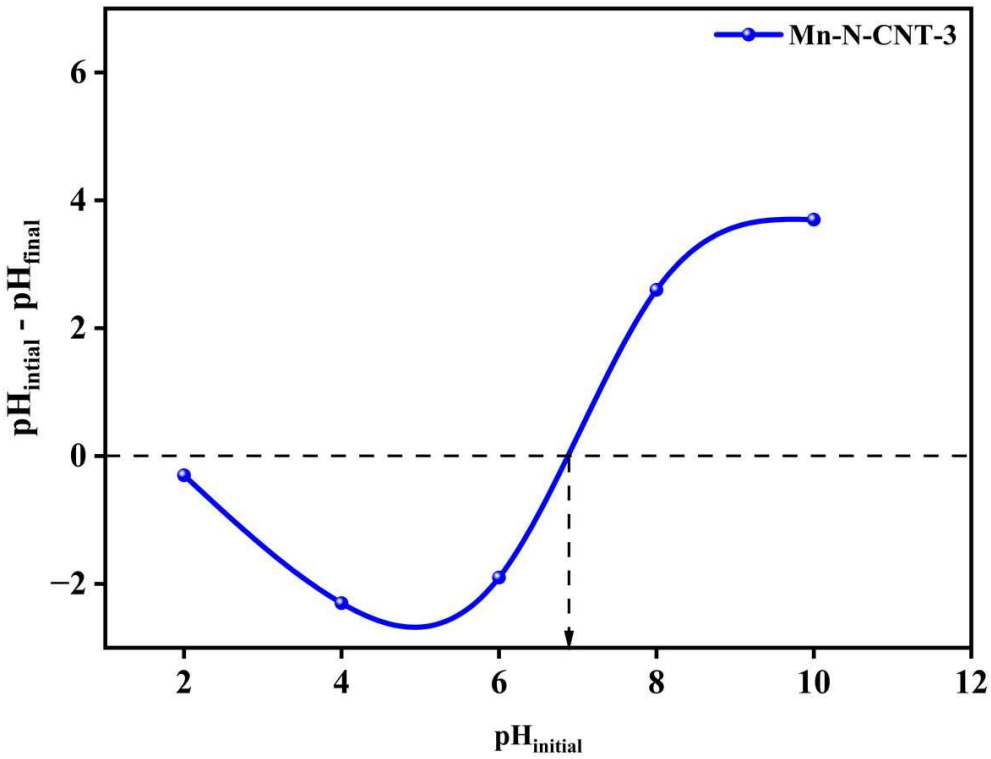

Figure 6. Point of zero charge of Mn-N-CNT-3

Identification of reactive oxygen species and catalytic mechanism

PMS can be activated through different mechanistic routes, including radical and nonradical pathways. As shown in **Figure 7**, quenching studies were performed using a series of quenchers, including EtOH, TBA, NaN_3, and $NaClO_4$, to probe the underlying mechanism and identify the key reactive oxygen species. Precisely, EtOH used to scavenge both $SO_4^{\bullet-}$ ($k_{EtOH+SO_4^{\bullet-}} = 1.6 - 7.8 \times 10^7 M^{-1}s^{-1}$ [37]) and $^{\bullet}OH$ ($k_{HO^{\bullet}+EtOH} = 1.2 - 1.8 \times 10^9\ M^{-1}s^{-1}$ [37]), while TBA used to scavenge $^{\bullet}OH$ ($k_{HO^{\bullet}+TBA} = 6.0 \times 10^8\ M^{-1}s^{-1}$ [50]) selectively. When EtOH and TBA were separately introduced into the Mn-N-CNT-3/PMS system, a noticeable decline in AYR degradation efficiency was observed. The rate constant decreased from 0.042 min^{-1} in the absence of scavengers to 0.027 min^{-1} with EtOH and 0.039 min^{-1} with TBA. The inhibitory effect suggests that both radicals play a role in AYR degradation. Subsequently, NaN_3 employed to quench $^1O_2$ ($k_{NaN_3 + {}^1O_2} = 2.2 \times 10^9 M^{-1}s^{-1}$ [51]) and $NaClO_4$ employed to quench nonradical electron transfer. When NaN_3 and $NaClO_4$ were separately introduced into the Mn-N-CNT-3/PMS system, AYR degradation rate reduced to 0.015 min^{-1} and 0.013 min^{-1}, respectively. The significant inhibitory effects observed with both scavengers imply that nonradical pathway, involving $^1O_2$ and nonradical electron transfer, also contributes to the overall degradation of AYR. Thus, the relative contributions of $^{\bullet}OH$, $SO_4^{\bullet-}$, $^1O_2$, and electron transfer in Mn-N-CNT-3/PMS system were quantified based on the stepwise reduction in the first-order degradation rate constants [52] and were determined to be 7.86 %, 31.83 %, 31.83 %, and 28.38 %, respectively. Based on the contribution percentage, it can be deduced that $SO_4^{\bullet-}$, $^1O_2$, and nonradical electron transfer are the major pathways for the degradation of AYR. The formation of metal-heteroatom coordination sites (e.g., Mn-pyridinic N) can modulate the local electronic structure by facilitating charge redistribution between the metal center and adjacent carbon atoms because they are electron-withdrawing groups [53]. This interaction promotes the adsorption and activation of PMS, thereby favoring the generation of nonradical reactive oxygen species such as $^1O_2$, which is consistent with the observed mechanistic trends. The generation of $SO_4^{\bullet-}$ can proceed through multiple pathways, including the cleavage of the O–O bond in PMS facilitated by delocalized π-electrons from sp2-hybridized carbon, as well as direct reactions between PMS and metal species (Eqs 2 – 3) [44]. These concurrent mechanisms contribute to its relatively higher abundance, thereby enabling $SO_4^{\bullet-}$ to play a dominant role in AYR degradation. In addition, the observed nonradical electron transfer pathway may be attributed to the formation of a metastable reactive complex between PMS and the catalyst surface (PMS*, which is an electron acceptor), a process that is facilitated by the electron-rich sp2-hybridized curved carbon framework [26]. These electron acceptor complexes will react with adsorbed AYR (electron donor) and result in the PMS consumption and AYR degradation. The relatively low contribution of $^{\bullet}OH$ in the Mn-N-CNT-3/PMS system can be attributed to its generation primarily through the electron-donating role of pyridinic N, which transfers lone-pair electrons to activate PMS (Eq 4) [54]. This indicates that $^{\bullet}OH$ formation is governed by the intrinsic activity of isolated pyridinic N sites, rather than arising from the synergistic interaction between Mn and N or the Mn-N coordination sites. Subsequently, AYR will undergo oxidation by reacting with the reactive oxygen species and form intermediates, CO_2, and H_2O (Eq 5).

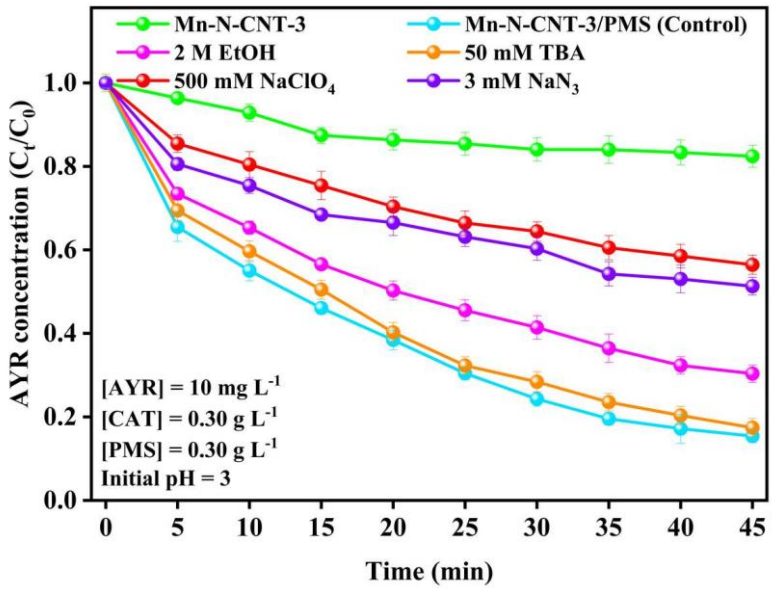

Figure 7. Effect of quenchers on the degradation of AYR

$$HSO_5^- + \pi - electron \rightarrow SO_4^{\bullet -} + OH^- \quad (2)$$
$$HSO_5^- + Mn^{2+} \rightarrow SO_4^{\bullet -} + OH^- + Mn^{3+} \quad (3)$$
$$HSO_5^- + e^- \rightarrow SO_4^{2-} + OH^{\bullet} \quad (4)$$
$$AYR + OH^{\bullet}/SO_4^{\bullet -}/{}^1O_2/PMS^* \rightarrow intermediates + H_2O + CO_2 \quad (5)$$

Reusability and toxicity assessments of Mn-N-CNT-3

As shown in **Figure 8**, the reusability of Mn-N-CNT in PMS to degrade AYR was evaluated through four consecutive cycles. AYR degradation rate reduced from 0.042 min^{-1} (84.6%) in the first cycle, to 0.025 min^{-1} (68.0%), 0.018 min^{-1} (56.5%), and 0.012 min^{-1} (41.6%) in the second, third, and fourth cycles, respectively. The decreasing trend of the removal rate could be due to (a) blockage of active sites by AYR and their intermediates and (b) loss of active sites for PMS activation via Mn leaching and N decomposition [55]. The blockage of active sites was found to be reversible and regeneration was achieved by thermally treating the catalyst (from the fourth cycle) at 450 °C under an oxygen-limited atmosphere. After regeneration, the catalyst was able to restore its performance, reaching a removal rate of 0.017 min^{-1} (53.5 %). Depending on national guidelines, the allowable concentration of Mn in drinking water typically ranges from 0.05 to 0.1 mg L^{-1} [56]. The amount of Mn leached (i.e., 0.02 mg L^{-1}) during the catalytic treatment was found to be below these regulatory limits, indicating that the process does not pose a risk of Mn contamination. When mineralization was examined, TOC removal was found to be much higher than anticipated. After 1 h of catalytic reaction, a mineralization efficiency of 52.1 % was obtained, showing that a large portion of AYR was broken down into smaller and more stable compounds (e.g., carbon dioxide, water, and inorganic ions). This result highlights that the Mn-N-CNT/PMS system is effective for decolourization and capable of driving substantial mineralization of AYR through the oxidative pathway.

Besides, the present study investigated the toxicity of catalytically treated AYR solution on the germinative and early growth responses (allelopathic impact) of Vigna radiata over a seven-day assay period (**Figure 9**). Three media were used for comparison, including distilled water, untreated AYR solution (10 mg L^{-1}), and catalytically treated AYR solution (after 1 h). After seven days, root and shoot lengths were measured and statistically evaluated. Seedlings grown in distilled water showed the highest root growth (4.17 ± 0.58 cm), followed closely by those in the treated AYR solution (3.68 ± 0.50 cm), while roots exposed to untreated AYR were considerably shorter (2.17 ± 1.00 cm). A similar pattern for shoots was observed, for example, 4.22 ± 1.00 cm in distilled water, 4.05 ± 0.65 cm in treated AYR, and only 1.22 ± 0.49 cm in untreated AYR. Statistical analysis confirmed that there was no significant difference ($p > 0.05$) between seedlings in distilled water and those in treated AYR, whereas untreated AYR caused a clear inhibition in both root and shoot development ($p < 0.05$). These findings indicate that catalytic treatment substantially lowers the toxicity of AYR and seedlings were able to grow almost normally in the treated solution.

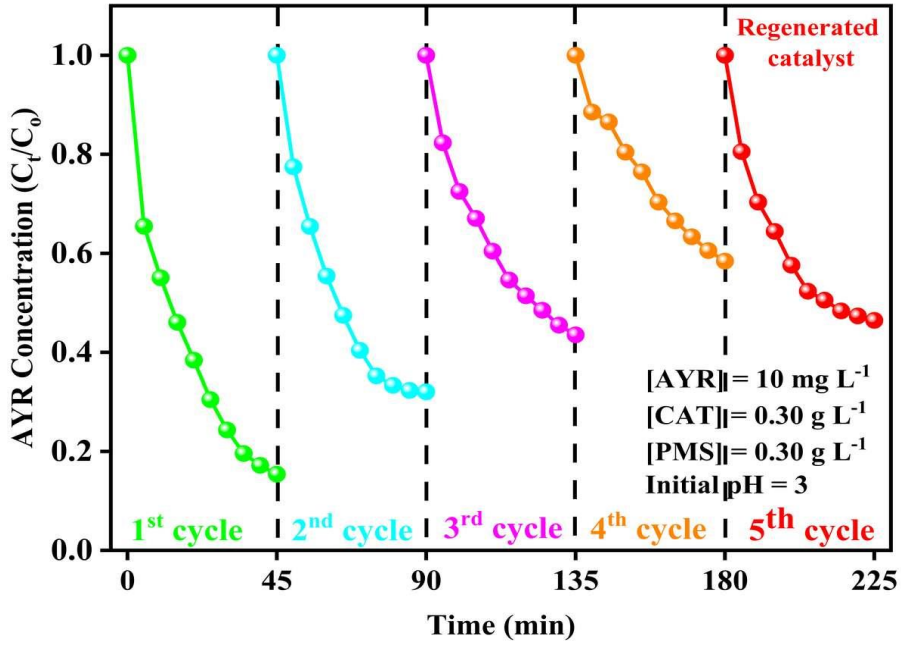

Figure 8. Reusability of Mn-N-CNT-3 in AYR degradation

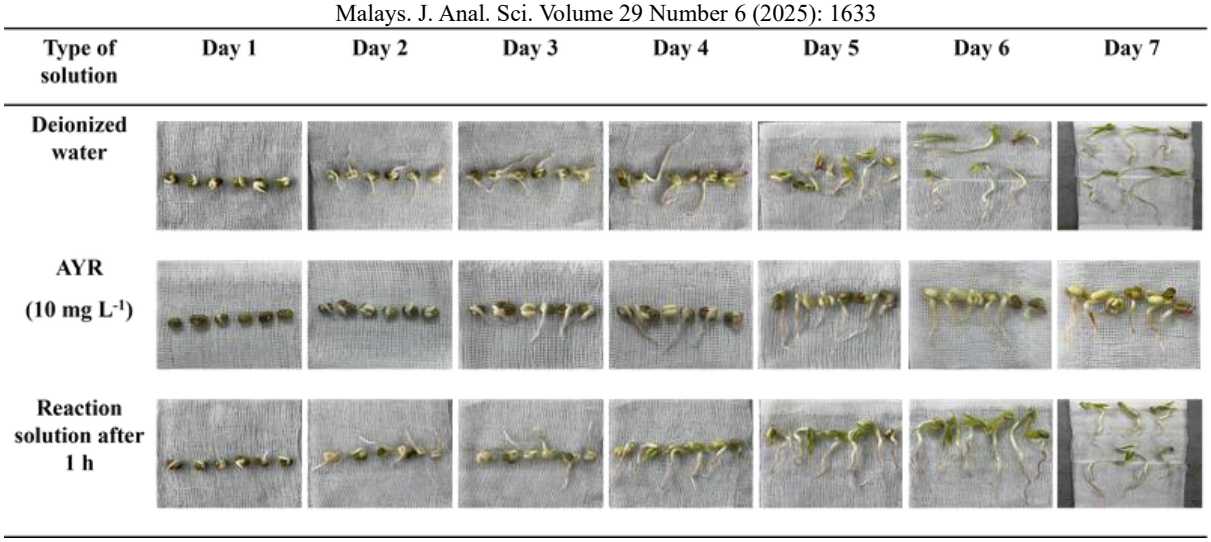

Figure 9. Phytotoxicity evaluation of the treated water using Vigna radiata seeds

Conclusion

This work demonstrated that Mn and N co-doping is an effective strategy to enhance the catalytic properties of carbon materials for PMS activation. Comparative evaluation of CNT and BC revealed that CNT co-doped with M and N exhibited superior catalytic activity, structural stability, and reusability, mainly due to their higher degree of graphitization, favorable nanotubular framework, and abundant Mn-N coordination sites. Mechanistic analysis confirmed that multiple reactive oxygen species contributed to AYR degradation, with $SO_4^{\bullet-}$ (31.8%), $^1O_2$ (31.8%), and electron transfer (28.4%) as the major pathways, while $^{\bullet}OH$ (7.9 %) played only a minor role. Despite a gradual decline in degradation over multiple cycles, the Mn-N-CNT-3 catalyst retained activity after regeneration, with Mn leaching levels below the regulatory limit. In addition to high decolorization, the system achieved substantial mineralization of AYR (i.e., 52.1% TOC removal), and phytotoxicity tests verified that the treated effluent was safe for seed germination and growth. Overall, this study not only underscores the advantages of tailoring carbon structures via Mn and N co-doping but also highlights the potential of CNT-based catalysts as sustainable and efficient PMS activators for wastewater treatment.

Acknowledgement

The Ministry of Higher Education Malaysia financially supported this work under the Fundamental Research Grant Scheme (FRGS, Grant number: FRGS/1/2023/STG04/USM/02/5). Icons from BioRender.com were used to prepare the figures in this manuscript.

References

1. Li, Y., Zhang, D., Chen, Q., Chao, C., Sun, J., Dong, S., and Sun, Y. (2022). Synthesis of rGO/g-C_3N_4 for methyl orange degradation in activating peroxydisulfate under simulated solar light irradiation. *Journal of Alloys and Compounds,* 907, 164500.
2. Li, X., Zhang, J., Jiang, Y., Hu, M., Li, S., and Zhai, Q. (2013). Highly efficient biodecolorization/ degradation of Congo Red and Alizarin Yellow R by chloroperoxidase from *Caldariomyces fumago*: Catalytic mechanism and degradation pathway. *Industrial and Engineering Chemistry Research,* 52(38), 13572–13579.
3. Binh, N. T., Khue, D. N., Van Chung, T., Hoa, N. T., and Quang, D. S. (2019). Kinetic modeling of degradation for Alizarin Yellow R by activated persulfate using Fe^0 (ZVI) under UV light. *Vietnam Journal of Chemistry,* 57(1), 46–51.
4. Ahmed, A., Usman, M., Yu, B., Ding, X., Peng, Q., Shen, Y., and Cong, H. (2020). Efficient photocatalytic degradation of toxic Alizarin Yellow R dye from industrial wastewater using biosynthesized Fe nanoparticles and study of factors affecting the degradation rate. *Journal of Photochemistry and Photobiology B: Biology,* 202, 111682.
5. Singh, G. B., Vinayak, A., Mudgal, G., and Kesari, K. K. (2024). Azo dye bioremediation: An interdisciplinary path to sustainable fashion. *Environmental Technology and Innovation,* 36, 103832.
6. Xiao, G., Xu, T., Faheem, M., Xi, Y., Zhou, T., Moryani, H. T., Bao, J., and Du, J. (2021). Evolution of singlet oxygen by activating peroxydisulfate and peroxymonosulfate: A review. *International Journal of Environmental Research and Public Health,* 18(7), 3344.
7. Li, H., Qin, X., Wang, K., Ma, T., and Shang, Y. (2024). Insight into metal-based catalysts for heterogeneous peroxymonosulfate activation: A critical review. *Separation and Purification Technology,* 333, 125900.

8. Brillas, E. (2024). Recent trends on the catalytic activation of peroxymonosulfate for the abatement of organic dyes in waters. *Journal of Environmental Chemical Engineering,* 12(4), 113191.
9. Xiao, S., Cheng, M., Zhong, H., Liu, Z., Liu, Y., Yang, X., and Liang, Q. (2020). Iron-mediated activation of persulfate and peroxymonosulfate in both homogeneous and heterogeneous ways: A review. *Chemical Engineering Journal,* 384, 123265.
10. Kohantorabi, M., Moussavi, G., and Giannakis, S. (2021). Innovations in metal- and carbon-based catalysts for heterogeneous peroxymonosulfate activation: Focus on radical versus nonradical degradation pathways. *Chemical Engineering Journal,* 411, 127957.
11. Huang, W., Xiao, S., Zhong, H., Yan, M., and Yang, X. (2021). Activation of persulfates by carbonaceous materials: A review. *Chemical Engineering Journal,* 418, 129297.
12. Pan, G., Wei, J., Xu, M., Li, J., Wang, L., Li, Y., Cui, N., Li, J., and Wang, Z. (2023). Insight into boron-doped biochar as an efficient metal-free catalyst for peroxymonosulfate activation: Role of –O–B–O– moieties. *Journal of Hazardous Materials,* 445, 130479.
13. He, L., Liao, G., Xie, Z., Liu, Y., and Yang, Y. (2025). Fe–N co-doped highly graphitized biochar for peroxymonosulfate activation toward degradation of persistent organic pollutants. *Environmental Research,* 286, 122786.
14. Huang, J., Zhu, Y., Bian, H., Song, L., Liu, Y., Lv, Y., Ye, X., Lin, C., and Li, X. (2023). Enhanced peroxydisulfate activation with B and Fe co-doped biochar from bark for rapid degradation of guaiacol. *Molecules,* 28(22), 7591.
15. Yang, X., Du, C., Chen, P., Zhang, S., Zhang, H., Xu, Q., and Zhuang, Z. (2025). Phosphorus-doped biochar loaded with cobalt nanoparticles for rapid acetaminophen degradation via peroxymonosulfate activation. *Applied Surface Science,* 713, 164309.
16. Huang, X., Yu, Z., Shi, Y., Liu, Q., and Fang, S. (2022). Highly efficient activation of peroxymonosulfate by Co,S co-doped bamboo biochar for sulfamethoxazole degradation. *Journal of Environmental Chemical Engineering,* 10(5), 108380.
17. Tao, Y., Sun, S., Hu, Y., Gong, S., Bao, S., Li, H., Zhang, X., Yuan, Z., and Wu, X. (2024). Activation of peroxymonosulfate by Fe,O co-embedded biochar for tetracycline degradation. *Catalysts,* 14(9), 556.
18. Sun, M., Fang, W., Liang, Q., Xing, Y., Lin, L., and Luo, H. (2024). Efficient acetaminophen degradation via peroxymonosulfate activation by Mn/N co-doped biochar. *Journal of Environmental Chemical Engineering, 12*(3), 112647.
19. Qu, G., Jia, P., Tang, S., Pervez, M. N., Pang, Y., Li, B., Cao, C., and Zhao, Y. (2024). Enhanced peroxymonosulfate activation via heteroatomic N-doping defects for BPA degradation. *Journal of Hazardous Materials,* 461, 132626.
20. Manickavasagam, G., He, C., Lin, K.-Y. A., Saaid, M., and Oh, W.-D. (2024). Advances and challenges of metal–heteroatom co-doped biochar as peroxymonosulfate activators. *Environmental Research,* 252, 118919.
21. Manickavasagam, G., He, C., Zhou, T., Hamidon, T. S., Hussin, M. H. H., Saaid, M., and Oh, W.-D. (2025). Stimulating catalytic activity of chars for norfloxacin removal via nitrogen and manganese functionalization. *Separation and Purification Technology,* 369, 133161.
22. Shende, R. C., Muruganathan, M., Mizuta, H., Akabori, M., and Sundara, R. (2018). Simultaneous synthesis of two nitrogen-rich carbon nanomaterials for all-solid-state symmetric supercapacitors. *ACS Omega,* 3(12), 17276–17286.
23. Shi, X., Huang, Z., Xu, J., Lin, S., Hong, Y., Zhang, Q., Xiao, J., and Hong, J. (2025). Co and N co-doped carbon nanotube catalysts for PMS activation. *Separation and Purification Technology,* 353, 128528.
24. Lim, X.-X., Low, S.-C., Tan, K. Q., Lin, K.-Y. A., Khoerunnisa, F., Lisak, G., and Oh, W.-D. (2024). Role of Ca in NiMoCa catalysts on carbon nanotube growth from face masks. *Journal of Analytical and Applied Pyrolysis,* 179, 106439.
25. Meng, H., Zhou, J., Nie, C., Li, W., Li, D., Zhang, Y., and Ao, Z. (2025). Mn-doped biochar induced peroxymonosulfate activation for phenol degradation. *Journal of Hazardous Materials,* 492, 138031.
26. Gasim, M. F., Veksha, A., Lisak, G., Low, S.-C. C., Hamidon, T. S., Hussin, M. H., and Oh, W.-D. (2023). Importance of carbon structure for N,S co-doping in ciprofloxacin removal. *Journal of Colloid and Interface Science,* 634, 586–600.
27. Fu, X., Li, Y., Cui, K., Liu, Y., and Lv, L. (2024). Mn and P co-doped biochar catalyst for persulfate degradation of tetracycline hydrochloride. *Journal of Environmental Chemical Engineering,* 12(6), 114228.
28. Manickavasagam, G., He, C., Zhou, T., Lin, K.-Y. A., Hamidon, T. S., Hussin, M. H., Saaid, M., and Oh, W.-D. (2024). Sustainable design of Co,N co-doped hydrochar as a PMS activator. *Chemical Engineering Journal,* 502, 157976.
29. Zhou, H., Kuang, Y., Gan, Y., Jiang, P., Pu, Y., and Yang, Y. (2025). Remediation of lead-contaminated soil using Fe–Mn–Ni layered double hydroxide biochar. *Chemical Engineering Journal Advances*, 100785.

30. Mutuma, M. K., Njogu, E. M., and Gichumbi, J. M. (2024). Synthesis and characterization of biochar–carbon nanotube composites for Rhodamine B adsorption. *IOSR Journal of Applied Chemistry,* 17(5): 27–42.
31. Jin, B., Wang, Q., Sainio, J., Saveleva, V. A., Jiang, H., Shi, J., Ali, B., Kallio, A.-J., Huotari, S., Sundholm, D., Han, N., and Kallio, T. (2024). Amorphous carbon-modulated quantum dot NiO for oxygen evolution. *Applied Catalysis B: Environment and Energy,* 358, 124437.
32. Chin, Y.-T., Manickavasagam, G., Lim, X.-X., Khoerunnisa, F., and Oh, W.-D. (2025). Biomass- and plastic-derived Co–N co-doped CNTs as PMS activators. *Journal of Water Process Engineering,* 72, 107635.
33. Zhang, M., Wen, Z., Zhang, L., Wang, Q., Zang, L., Feng, Q., Gu, Y., Wang, W., Ma, K., Zhang, H., Ji, D., Liu, J., Shi, X., and Yu, F. (2025). Radical and nonradical PMS activation by $Fe_{1-x}S$/lignin biochar nanocomposites. *Chemical Engineering Journal,* 520, 166153.
34. Li, G., Cao, X., Meng, N., Huang, Y., Wang, X., Gao, Y., Li, X., Yang, T., Li, B., Zhang, Y., Lyu, X., and Liang, Y. (2022). Fe_3O_4-supported biochar for PMS activation in urea degradation. *Chemical Engineering Journal,* 433, 133595.
35. Jeong, W.-G., Kim, J.-G., Alshawabkeh, A. N., Larese-Casanova, P., Lim, J., and Baek, K. (2025). Electrochemical activation of PMS with biochar for p-nitrophenol removal. *Journal of Water Process Engineering,* 71, 107276.
36. Chen, X., Oh, W.-D., Hu, Z.-T., Sun, Y.-M., Webster, R. D., Li, S.-Z., and Lim, T.-T. (2018). Enhancing sulfacetamide degradation by PMS activation with N-doped graphene. *Applied Catalysis B: Environmental,* 225, 243–257.
37. Zhu, S., Huang, X., Ma, F., Wang, L., Duan, X., and Wang, S. (2018). Catalytic removal of aqueous contaminants on N-doped graphitic biochars. *Environmental Science and Technology,* 52(15), 8649–8658.
38. Xiao, Y., Mu, J., Peng, Q., Feng, J., Zhou, B., Zhang, N., and Liu, B. (2025). Oxygen-vacancy-enhanced PMS activation via carbon-hybrid defective Mn_2O_3. *Journal of Environmental Chemical Engineering,* 13(1), 115032.
39. Liu, T., Li, C., Chen, X., Chen, Y., Cui, K., Wang, D., and Wei, Q. (2024). PMS activation by Fe@N co-doped biochar for sulfamethoxazole degradation. *International Journal of Molecular Sciences,* 25(19), 10528.
40. Guo, L., Liu, D., Han, R., Yin, A., Gong, G., Li, S., Chen, R., Yang, J., Liu, Z., and Zhi, K. (2025). Advances in persulfate activation by carbon-based materials. *Crystals,* 15(5), 432.
41. Zhong, C., Zhang, S., Yang, S., Yuan, B., Xu, Q., Xie, Z., and Du, C. (2023). Mo,N co-doped iron biochar activating PMS for BPA degradation. *Chemical Engineering Journal,* 466, 143298.
42. Chen, W., Lei, L., Zhu, K., He, D., He, H., Li, X., Wang, Y., Huang, J., and Ai, Y. (2023). PMS activation by Fe–N–S co-doped carbocatalyst. *Journal of Environmental Sciences,* 129, 213–228.
43. Wu, Q., Zhang, Y., Meng, H., Wu, X., Liu, Y., and Li, L. (2024). Cu/N co-doped biochar activating PMS for selective paracetamol degradation. *Chemosphere,* 357, 141858.
44. Xue, Y., Kamali, M., Costa, M. E. V., Thompson, I. P., Huang, W., Rossi, B., Appels, L., and Dewil, R. (2024). PMS activation by Fe,N co-doped walnut shell biochar. *Environmental Pollution,* 355, 124018.
45. Kong, L., Zhu, M., and Zhan, J. (2025). Nitrogen-doped biochar aerogels as efficient PMS activators. *Nanomaterials,* 15(11), 865.
46. Huong, P. T., Jitae, K., Al Tahtamouni, T. M., Le Minh Tri, N., Kim, H.-H., Cho, K. H., and Lee, C. (2020). Biochar-derived PMS activation for oxidation of organic contaminants. *Journal of Water Process Engineering,* 33, 101037.
47. Yan, B., Li, Q., Chen, X., Deng, H., Feng, W., and Lu, H. (2022). O_3/PMS advanced oxidation technology for highly concentrated organic wastewater. *Separations, 9*(12), 444.
48. Wu, L., Lin, Y., Zhang, Y., Wang, P., Ding, M., Nie, M., Yan, C., and Chen, S. (2021). $Ca(OH)_2$-mediated PMS activation for bisphenol S degradation. *RSC Advances,* 11(53), 33626–33636.
49. Mashentseva, A. A., Aimanova, N. A., Parmanbek, N., Temirgaziyev, B. S., Barsbay, M., and Zdorovets, M. V. (2022). Plant-mediated synthesis of ZnO nanoparticles for Alizarin Yellow R removal. *Nanomaterials,* 12(19), 3293.
50. Neta, P., Huie, R. E., and Ross, A. B. (1988). Rate constants for reactions of inorganic radicals in aqueous solution. *Journal of Physical and Chemical Reference Data,* 17(3), 1027–1284.
51. Basu-Modak, S., and Tyrrell, R. M. (1993). Singlet oxygen: A primary effector in the ultraviolet A/near-visible light induction of the human heme oxygenase gene. *Cancer Research,* 53(19), 4505–4510.
52. Wang, J., Shen, M., Wang, H., Du, Y., Zhou, X., Liao, Z., Wang, H., and Chen, Z. (2020). Red mud-modified sludge biochar for the activation of peroxymonosulfate: Singlet oxygen-dominated mechanism and toxicity prediction. *Science of the Total Environment, 740*, 140388.
53. Wu, S., Liu, H., Yang, C., Li, X., Lin, Y., Yin, K., Sun, J., Teng, Q., Du, C., and Zhong, Y. (2020). High-performance porous carbon catalysts doped with iron and nitrogen for degradation of bisphenol F via peroxymonosulfate activation. *Chemical Engineering Journal,* 392, 123683.

54. Xu, L., Fu, B., Sun, Y., Jin, P., Bai, X., Jin, X., Shi, X., Wang, Y., and Nie, S. (2020). Degradation of organic pollutants by Fe/N co-doped biochar via peroxymonosulfate activation: Synthesis, performance, mechanism, and potential for practical application. *Chemical Engineering Journal,* 400, 125870.
55. Gan, Y., Zhu, K., Xia, W., Zhu, S., Tong, Z., Chen, W., Wang, Y., and Lin, B. (2022). Strongly coupled Fe/N co-doped graphitic carbon nanosheets/carbon nanotubes for rapid degradation of organic pollutants via peroxymonosulfate activation: Performance, mechanism, and degradation pathways. *Separation and Purification Technology,* 302, 122113.
56. Patil, D. S., Chavan, S. M., and Oubagaranadin, J. U. K. (2016). A review of technologies for manganese removal from wastewaters. *Journal of Environmental Chemical Engineering,* 4(1), 468–487.